

Parallel Algorithms and Software for Nuclear, Energy, and Environmental Applications. Part II: Multiphysics Software

Derek Gaston¹, Luanjing Guo², Glen Hansen^{3,*}, Hai Huang², Richard Johnson¹, Dana Knoll⁴, Chris Newman⁴, Hyeong Kae Park⁴, Robert Podgorney², Michael Tonks¹ and Richard Williamson¹

¹ Nuclear Science and Technology, Idaho National Laboratory, Idaho Falls, ID 83415, USA.

² Energy and Environment Science and Technology, Idaho National Laboratory, Idaho Falls, ID 83415, USA.

³ Multiphysics Simulation Technologies Dept. (1444), Sandia National Laboratories, Albuquerque, NM 87185, USA.

⁴ Fluid Dynamics and Solid Mechanics Group (T-3), Los Alamos National Laboratory, Los Alamos, NM 87545, USA.

Received 9 October 2010; Accepted (in revised version) 14 July 2011

Available online 1 March 2012

Abstract. This paper is the second part of a two part sequence on multiphysics algorithms and software. The first [1] focused on the algorithms; this part treats the multiphysics software framework and applications based on it. Tight coupling is typically designed into the analysis application at inception, as such an application is strongly tied to a composite nonlinear solver that arrives at the final solution by treating all equations simultaneously. The application must also take care to minimize both time and space error between the physics, particularly if more than one mesh representation is needed in the solution process. This paper presents an application framework that was specifically designed to support tightly coupled multiphysics analysis. The Multiphysics Object Oriented Simulation Environment (MOOSE) is based on the Jacobian-free Newton-Krylov (JFNK) method combined with physics-based preconditioning to provide the underlying mathematical structure for applications. The report concludes with the presentation of a host of nuclear, energy, and environmental applications that demonstrate the efficacy of the approach and the utility of a well-designed multiphysics framework.

*Corresponding author. *Email addresses:* Derek.Gaston@inl.gov (D. Gaston), Luanjing.Guo@inl.gov (L. Guo), gahanse@sandia.gov (G. Hansen), Hai.Huang@inl.gov (H. Huang), Rich.Johnson@inl.gov (R. Johnson), nol@lanl.gov (D. Knoll), cnewman@lanl.gov (C. Newman), hkpark@lanl.gov (H. K. Park), Robert.Podgorney@inl.gov (R. Podgorney), Michael.Tonks@inl.gov (M. Tonks), Richard.Williamson@inl.gov (R. Williamson)

AMS subject classifications: 65M12, 65M60, 65Y05, 65Z05, 65H10

Key words: Multiphysics simulation, Jacobian-free Newton Krylov, finite element applications, physics-based preconditioning.

1 Introduction

This paper describes an evolving software framework MOOSE [2] which utilizes the algorithmic framework presented in Part I [1] to enable rapid development of multiphysics engineering analysis tools. Further, it presents several applications based on the MOOSE framework that support high fidelity analysis of various nuclear, energy, and environmental problems.

BISON [3] is a nuclear fuel performance code that is designed to analyze how fuel behaves within a nuclear reactor. It is a fully coupled multiphysics application that combines thermomechanics of the fuel and protective cladding material with specialized models that describe how the fuel (and cladding) ages as it is subjected to thermal stresses and irradiation. This fuel performance application is particularly interesting in that it is also a fully coupled multiscale application. This analysis capability employs a separate calculation at a much lower length scale (the *mesoscale*) that computes how the fuel material behaves under irradiation conditions, and how the thermal conductivity, stress, and strain behaves at this scale. This information is then bridged up to the BISON finite element code to describe the bulk fuel behavior. The model is strongly coupled in that the thermal profile of the fuel (calculated at the large scale) affects the susceptibility of the fuel material to irradiation processes.

PRONGHORN [4] is a reactor core simulator for Pebble-Bed Reactors (PBRs) that models neutronics, fluid dynamics, and heat conduction within the solid components of the reactor. It is also a fully coupled application that examines the dynamics of these three coupled effects in reactor geometry.

FALCON is under development to support the analysis of geothermal reservoirs and geothermal systems, and considers multiphase fluid flow, energy transport, and deformation of the subsurface in such systems. RAT is also a subsurface analysis code designed to simulate single phase flow and reactive geochemistry. Both of these applications are designed for fully coupled simulation and use the MOOSE framework.

This part begins with a description of the MOOSE framework.

2 Software and results

2.1 MOOSE

The Multiphysics Object Oriented Simulation Environment is a computational framework created at the Idaho National Laboratory to enable rapid development of new sci-

entific simulation capabilities [2]. MOOSE was developed specifically for tackling the strongly coupled multiphysics problems that are prevalent in nuclear engineering and has since been utilized in many other fields. The core solution algorithm in MOOSE is the preconditioned Jacobian-free Newton Krylov method (JFNK), that typically provides rapid nonlinear convergence for a fully coupled set of partial-differential equations. Use of this algorithm has allowed for the development of a robust and extensible architecture that supports the construction of complex simulation tools in a fraction of the time previously thought necessary.

MOOSE was created as a framework for the rapid development of parallel engineering analysis tools. It was developed using modern software engineering principles and practices, and had to provide compelling capabilities in a manner that lowered the maintenance and update costs for applications developed using it. To support these requirements, MOOSE is a fully object-oriented library, with each portion of functionality decoupled from all others. This isolation of capability into well defined modules allows for both the framework and applications based on it to grow without the cost usually associated with large scientific software engineering endeavors.

Multiphysics analysis usually involves problems with a large number of degrees of freedom (DOFs), therefore solution strategies using parallel programming paradigms are often necessary. MOOSE incorporates multiple parallel solution capabilities including both Message Passing Interface (MPI) and threading using the Intel Threading Building Blocks (TBB). Having multiple parallel options allows MOOSE based applications to run efficiently on multicore workstations, laptops and supercomputers. The functionality that implements parallel execution is fully hidden from application developers, enabling the scientists and engineers developing applications to focus on the problem they wish to solve instead of parallel programming practices. Further, having all of the parallel functionality within the framework also enables advanced research into parallel programming capabilities by the framework developers, without disrupting the applications.

MOOSE has been developed using a multilayer model. It uses several open-source libraries from selected universities and national laboratories. In particular, the libMesh finite-element framework developed by the CFDLab at the University of Texas in Austin provides the core set of parallel finite-element capability [5]. Coupled with linear and nonlinear solvers from both the PETSc [6] and Trilinos [7] projects along with other packages such as Hypre [8], MOOSE provides a modular, structured interface to significant parallel computational capability.

MOOSE utilizes a semidiscrete method where the problem is discretized spatially using the finite element method and temporally using traditional finite difference methods. The finite element discretization can be realized in MOOSE via first and second order Lagrange, arbitrary order C^0 hierarchic, C^1 continuous and discontinuous finite element families. Element types consist of the standard geometric types: triangles, quadrilaterals, tetrahedrals, hexahedrals, prisms and pyramids. Specific details for finite element methods can be found in [9] and [10]. Time integration methods include implicit Euler, Crank-Nicolson and second order backward difference [11].

Accuracy and cost of the simulation are determined by mesh size. Regions with discontinuities, shocks, steep gradients and variation in spatial scale require greater mesh resolution. MOOSE utilizes h mesh adaptivity (cell refinement) [12] and [13]. Mesh adaptivity is typically driven by some local estimation of error, the mesh is enriched where the local estimated error is high and coarsened where the local estimated error is low. MOOSE utilizes a gradient jump error indicator that is derived from [14]. MOOSE includes the capability for physics independent and physics dependent error estimation [15], where in a coupled problem different weights can be assigned to the error indicator of each variable. Similar to spatial adaptivity, MOOSE has the capability for adaptive time step control, where the time step size is adjusted to control temporal error [11].

The resulting nonlinear system of equations is solved using the preconditioned Jacobian-free Newton-Krylov method described in Part I [1]. The examples in this paper utilize first order Lagrange finite element spatial discretization, implicit Euler temporal discretization and h adaptivity based on the gradient jump estimator.

The modular, interchangeable interfaces defined in MOOSE allow scientific simulation tools to be developed using fewer lines of code as compared to other strategies. Many applications (including those discussed below) can be developed with fewer than 1,000 lines of code. Those 1,000 lines enable parallel solution of multidimensional, fully-coupled systems of partial differential equations. This ability to keep the number of lines of code to a minimum creates an environment where scientists and engineers can focus on the physics they are interested in without the overhead typically associated with the use of advanced parallel solution capabilities.

2.2 BISON

BISON [3], is a macroscale nuclear reactor fuel performance code developed using MOOSE. It is designed for fully-coupled multidimensional steady and transient analysis based upon a thermomechanical physics core. This discussion summarizes the current status of BISON and demonstrates the code's capability and performance when applied to the analysis of both light water reactor fuel and TRISO fuel particles.

2.2.1 Governing equations

The BISON governing relations currently consist of fully-coupled partial differential equations for energy, species, and momentum conservation. The energy balance is given in terms of the heat conduction equation

$$\rho C_p \frac{\partial T}{\partial t} + \nabla \cdot \mathbf{q} - e_f \dot{F} = 0, \quad (2.1)$$

where T , ρ and C_p are the temperature, density and specific heat, respectively, e_f is the energy released in a single fission event, and \dot{F} is the volumetric fission rate. \dot{F} can be prescribed as a function of time and space, or input from a separate neutronics calculation.

The heat flux is given as

$$\mathbf{q} = -k\nabla T, \quad (2.2)$$

where k denotes the thermal conductivity of the material.

Species conservation is given by

$$\frac{\partial C}{\partial t} + \nabla \cdot \mathbf{J} + \lambda C - S = 0, \quad (2.3)$$

where C , λ , and S are the concentration, radioactive decay constant, and source rate of a given species, respectively. The mass flux \mathbf{J} is specified as

$$\mathbf{J} = -D\nabla C, \quad (2.4)$$

where D is the diffusion coefficient; this definition has been used to simulate fission product transport within the fuel. Also implemented in BISON is a hyperstoichiometric model for oxygen diffusion in UO_2 fuel as described in [3]. In this case \mathbf{J} denotes the oxygen flux in the hyperstoichiometric regime with,

$$\mathbf{J} = -D \left(\nabla C - \frac{CQ^*}{FRT^2} \nabla T \right), \quad (2.5)$$

where D is diffusivity, F is the thermodynamic factor of oxygen, Q^* is the heat of transport of oxygen, and R is the universal gas constant.

Momentum conservation is prescribed assuming static equilibrium at each time increment using Cauchy's equation,

$$\nabla \cdot \mathbf{T} + \rho \mathbf{f} = 0, \quad (2.6)$$

where \mathbf{T} is the Cauchy stress tensor and \mathbf{f} is the body force per unit mass (*e.g.*, gravity). The displacement field $\mathbf{u}(\mathbf{x}, t)$, which is the primary solution variable, is connected to the stress field via the strain, through a constitutive relation. In the current BISON configuration, small-deformation is assumed with the strain a rank-two tensor whose components are

$$e_{ij} = \frac{1}{2}(u_{i,j} + u_{j,i}). \quad (2.7)$$

2.2.2 Constitutive relations

Focusing initially on UO_2 fuel, constitutive models have been developed and tested to describe temperature and burnup dependent thermal properties, diffusion coefficients, elasticity, fission product swelling, densification, and fission gas release.

The temperature-dependent thermal conductivity of unirradiated UO_2 is defined using an empirical equation suggested by Fink [16]. This relationship is then modified to account for the effects of irradiation and porosity using a series of multipliers, as outlined in detail by Lucuta *et al.* [17].

Diffusion coefficients for fission products are strongly temperature dependent and defined using an Arrhenius form [18]

$$D(T) = \sum_i D_{0,i} \exp\left(\frac{-Q_i}{RT}\right), \quad (2.8)$$

where D_0 is a pre-exponential factor and Q is the activation energy.

Linear thermoelastic material response is prescribed using the generalized Hooke's law

$$T_{ij} = c_{ijkl} e_{kl} - \alpha_{ij} (T - T_0), \quad (2.9)$$

where c_{ijkl} are the elastic modulus and α_{ij} the thermal expansion tensors, respectively. For isotropic behavior, this relation can be defined in terms of two elastic constants (typically Young's modulus and the Poisson's ratio) and the linear coefficient of thermal expansion. Swelling as a result of both solid and gaseous fission products is included using the empirical relations from MATPRO [19]. Densification of initial fuel porosity is computed using the ESCORE empirical model [20].

Fission gas release is computed using the Forsberg-Masih [21] analytical model, which is based on diffusion of fission gas atoms within an assumed spherical fuel grain. This model incorporates a two-stage approach to predict gas release. The first stage simply computes gas diffusion to the grain boundary which, for the BISON implementation, is governed by the three term Turnbull diffusion coefficient [22]. The second stage utilizes time-dependent boundary conditions to determine grain boundary gas accumulation, resolution, saturation, and release parameters. Release from the grain boundaries is controlled using a grain boundary saturation criterion.

2.2.3 Applications

In an early LWR application, BISON was used to simulate thermomechanics and oxygen diffusion in a single fuel pellet [3]. It was demonstrated that fully-coupled three dimensional fuel performance solutions were quite plausible and efficient using the JFNK approach.

In a more recent LWR application, the thermomechanical behavior of a partial fuel rod was considered. The rod included 100 discrete fuel pellets and associated cladding, all in three dimensions. Because contact capabilities are not fully implemented, the pellet-clad gap was meshed in this demonstration problem. The problem was simulated using hundreds of processors, demonstrating the powerful parallel computing ability of the MOOSE framework.

Fig. 1 shows results from this simulation. The top figure is a perspective view of the rod, with colors corresponding to axial displacement of the pellets. The lower left figure shows the magnified radial displacement at the outer surface of the cladding. Note the ridged, "bamboo" appearance of the rod, which results from cladding coming into contact with the fuel pellets that have deformed into an hourglass shape due to thermal expansion. The lower center figure shows the computed temperature profile across the

fuel rod. Note that fuel centerline temperatures are rather low in this demonstration calculation simply because a low fission rate was specified. The lower right figure shows the radial displacement of the fuel rod components viewed on a cross section through the center of the rod.

BISON was the first MOOSE-based application built; development started on it in May 2008. Major development activities continue with the addition of a general plasticity model that describes the zircalloy metal cladding (Zr-4), a model for radiation-induced creep, and general damage. Secondly, a sophisticated pellet cladding interaction (PCI) model is under development that will be able to predict the correct displacements, stresses, and strains at the pellet cladding interface given the relative displacements of a given location on a pellet with respect to the cladding. This model is challenging due to the desire to robustly accommodate large displacement scenarios (recall that implicit time integration is employed in BISON), and during parallel execution. Further, mechanics to describe the thermal stress induced fracturing of the UO_2 pellets will soon be implemented in BISON; the contact method must properly treat the complex multiple surface topologies that will be present. The initial thermal implementation is discussed in [23], an outline of the coupling of the thermal and mechanical physics as well as the JFNK nonlinear solver is developed in [24].

BISON has also been applied to TRISO-coated fuel particles (the fuel form used in high temperature gas-cooled reactors) by investigating coupled heat transfer and fission product transport for a variety of fuel particle configurations [25]. For this study, the above equation set is simplified to include only (2.1)-(2.4) and (2.8). The particular case described here considers cesium transport from a failed particle.

The geometry, mesh, materials, and boundary conditions for the calculation are shown in Fig. 2(a). The particle outside diameter is 0.855 mm. Eighth symmetry was achieved by setting the heat and mass flux to zero on the three symmetry planes. Cesium is uniformly generated in the UO_2 fuel based on an assumed constant particle power of 50 mW. Since the SiC layer represents the main impediment to cesium release from the particle, simple flaws were created by modifying the material properties of groups of finite elements through this layer. Simulations were performed for four different geometries by first considering a single flaw (flaw 1 in Fig. 2(a)) and then successively adding the second, third, and fourth flaws identified in the figure. Note that the initial mesh is rather coarse in the vicinity of the flaws, thus the powerful adaptive mesh refinement capability in MOOSE was employed. Mesh refinement was driven by estimated error in the gradient jump of cesium concentration.

Fig. 2(b) shows the computed cesium concentration contours for the four-flaw geometry after approximately 510 days of irradiation. The local “venting” of cesium through the flaws is evident. Note that the mesh is significantly refined to resolve the concentration gradients in the vicinity of the flaws and the IPyC/SiC interface, with limited or no refinement throughout the rest of the domain.

Fig. 3 shows the effect of the SiC flaws by comparing the predicted fractional release (cesium released/cesium produced) for an undamaged particle and the four flawed ge-

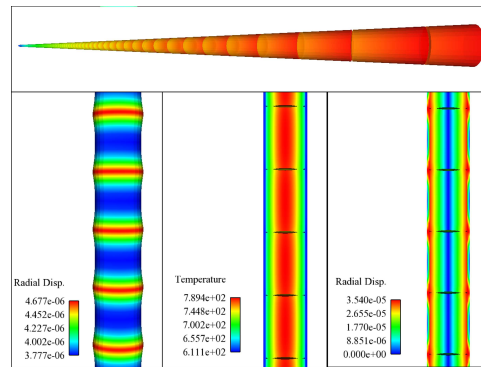


Figure 1: Panel of results from a 100 pellet fuel rod simulation. The upper figure shows a perspective view of the rod, with colors corresponding to axial displacement of the pellets. The lower left figure shows the magnified radial displacement of the outer surface of the cladding, showing the displacement imparted by the pellets into the cladding. The lower center figure shows the temperature profile across the fuel rod, and the lower right figure the radial displacement viewed on a cross section through the center of the rod. Simulation was performed in April 2010.

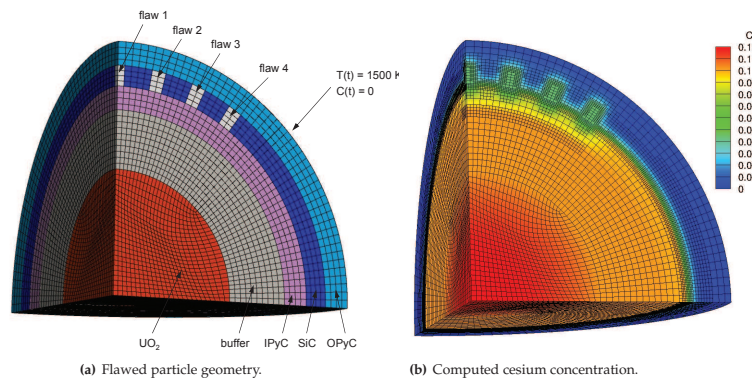


Figure 2: Figure (a) shows the geometry, mesh, materials, and boundary conditions for the flawed particle calculation. IPyC and OPyC refer to the inner and outer pyrolytic carbon layers, respectively, in the particle. Figure (b) shows the computed cesium concentration ($\mu\text{mol}/\text{mm}^3$) for the four-flaw geometry after 510 days of irradiation.

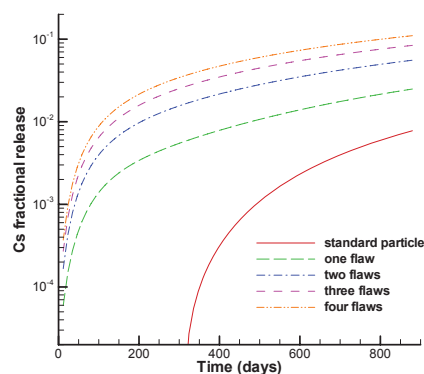


Figure 3: Comparison of the cesium fraction release histories for an undamaged particle and the four SiC flaw geometries.

ometries. Even a single flaw results in significant cesium release early in fuel life, with the four-flaw simulation predicting over 10% release by the end of fuel life.

2.3 Scale bridging

The performance of fuel within a reactor is largely dependent on microstructural changes that occur due to radiation damage. These changes include pore nucleation, growth and migration, grain growth, and fission gas segregation. The radiation-induced microstructural evolution impacts basic material properties such as thermal conductivity, density and the elastic constants. While the effect of radiation on basic properties are typically considered in fuel performance codes using empirical fits of experimental data [26], this approach can interpolate within understood conditions but not accurately extrapolate to new conditions. A phenomenological model of reactor fuel must directly consider microstructural changes to accurately describe the macroscale behavior.

Various models have been developed that predict radiation-induced microstructural evolution. These models represent the microstructure at the mesoscale, resolving grains, voids and bubbles but not individual atoms nor point defects. [27] and [28] use the Monte Carlo Potts model to describe the evolution of microstructure with existing voids and bubbles. [29] develop a phase field model to predict the nucleation and growth of voids during irradiation. Mesoscale models also provide a mechanism for predicting the effect of irradiation on material properties such as thermal conductivity [30]. However, the computational expense of employing a mesoscale approach to model a macroscale fuel pellet is prohibitively large, due to the large number of degrees of freedom involved.

The effect of radiation-induced microstructural evolution can be considered at the macroscale by coupling mesoscale calculations to a finite element (FE) fuel performance code, such as BISON. Two basic approaches exist for multiscale coupling. In hierarchical coupling, mesoscale simulations are conducted to determine constitutive relationships describing the effect of radiation on bulk material properties. These relationships are then included in the fuel performance code. In concurrent coupling, mesoscale simulations are directly coupled to the macroscale code at every integration point and at every time step. Concurrent coupling is significantly more computationally expensive than hierarchical coupling, but it provides direct access to microstructural information throughout the macroscale, can account for complex operating conditions, and can capture history dependence of the microstructural evolution. Primarily, hierarchical coupling is ideal for large macroscale simulations while concurrent coupling is appropriate for smaller macroscale problems that required a large degree of detail and accuracy. Because it is computationally more complex, we have focused our initial efforts on concurrent coupling.

2.3.1 Concurrent coupling

We have developed a general methodology to couple a mesoscale microstructure model to a macroscale fuel performance code. The algorithm is summarized here, though it

is discussed in more detail in [31]. In the algorithm, a fuel pellet is represented with a macroscale FE model. At each time step, the JFNK algorithm is used to solve the nonlinear system. During the nonlinear convergence process, the mesoscale model evolves the microstructure at the current conditions at each integration point and determines effective material parameter values \mathbf{p}^e . These parameters are fit with a polynomial surface, which provides the parameter values $\mathbf{p}_{\text{fit}}^e$ to the FE model. This process is repeated, providing more calculated values to improve the fit, until the solution converges. The evolved mesoscale microstructure at each integration point becomes the initial microstructure at the next time step. See Fig. 4 for a schematic of the proposed multiscale methodology.

To demonstrate this multiscale approach, a simplified multiscale model of an irradiated fuel pellet is presented. The dished pellet has a diameter of 8.26 mm and a height of 6.75 mm. In the simple model, the steady-state temperature profile is determined in the fuel pellet using BISON for a single nonlinear solution. At each integration point, the mesoscale phase field model from [29] evolves the microstructure at the current integration point temperature and calculates the effective thermal conductivity. This value is then used by the FE model to determine the temperature for the next nonlinear iteration. Both the macroscale fuel pellet representation and the mesoscale model of the fuel material are significant simplifications of actual fuel pellet behavior, as the purpose of this preliminary work is to develop and demonstrate the multiscale methodology and not to develop an accurate fuel model. This initial demonstration is described in more detail in [31].

To investigate the numerical performance of the multiscale model, two simulations are conducted, one to evaluate the nonlinear convergence and the other the parallel scalability of the approach. The first simulation considers the pellet with a constant temperature $T_C = 810$ K on the outer circumference and a uniform applied heat source $Q = 200$ MW/m³. The pellet is discretized with 720 elements and the temperature distribution throughout the pellet is calculated using the multiscale model. Fig. 5(a) shows the strong nonlinear convergence obtained by the proposed multiscale JFNK approach on this representative problem. To evaluate the parallel scalability of the basic scale-bridging methodology suggested here, the pellet is maintained at a constant temperature $T = 810$ K. For this simulation, the pellet is discretized with 5760 elements and the mesoscale model is evaluated once per integration point, as only one iteration is required. The “strong” parallel scalability is investigated, *i.e.*, the problem size is unchanged while it is solved using an increasing number of processors ranging from 3 to 1440. The method exhibits near ideal scalability, as shown in Fig. 5(b). This result is not surprising, as each mesoscale calculation is independent from the others and they run concurrently within each JFNK function evaluation.

To investigate the physical behavior predicted by the mesoscale model, the fuel pellet simulation used to investigate the nonlinear convergence is repeated, *i.e.*, the temperature profile is determined in a fuel pellet of height $h = 6.75$ mm and diameter $d = 8.26$ mm with a constant temperature $T_C = 810$ K on the outer circumference and a uniform applied heat

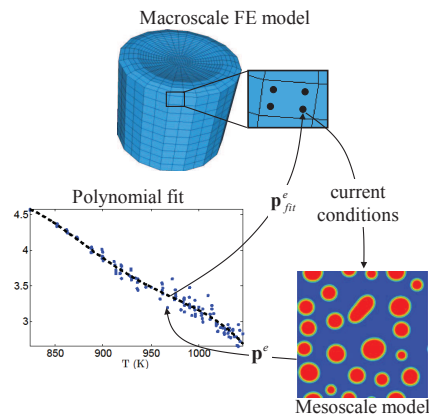


Figure 4: Schematic of the proposed multiscale methodology. At the current conditions, the mesoscale model determines effective parameter values p^e which are fit with a polynomial surface at each nonlinear iteration. The macroscale FE model obtains values of p_{fit}^e from the latest fit.

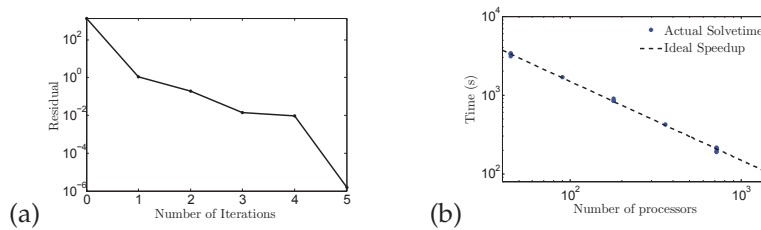


Figure 5: Numerical performance of the multiscale model, with (a) Plot of the nonlinear residual vs. number of Newton iterations during the multiscale simulation. The model exhibits good nonlinear convergence. Figure (b) shows the parallel scalability of the multiscale calculation. The problem size is kept constant as the number of processors is increased, thus this data provides a metric of the nearly ideal strong scaling of the multiscale approach.

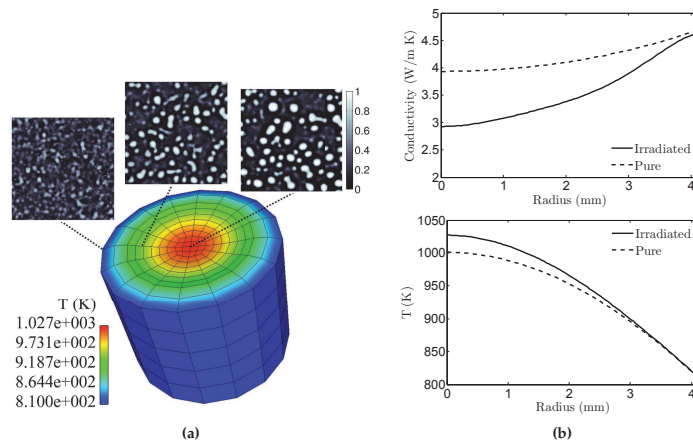


Figure 6: (a) Fuel pellet temperature profile, where color corresponds to temperature. Snapshots above the pellet show vacancy concentration in the microstructure computed by the mesoscale model at the indicated radial positions. (b) Comparison between the radial thermal conductivity (top) and the temperature profile (bottom) in an irradiated fuel pellet and in a pure pellet. Values are measured at a height $z=3.825$ mm from the base of the pellet.

source $Q=200 \text{ MW/m}^3$. The pellet is discretized with 720 elements. Fig. 6(a) shows both the temperature profile within the fuel pellet and plots of the mesoscale vacancy concentration at three radial positions within the pellet. From these results, it is evident that the void formation has a strong radial dependence; at the pellet center, many large voids surrounded by vacancy-depleted zones have formed; at mid-radius, a larger number of small voids have formed; on the outer circumference, only a few small voids are present (see [32] for experimental observations showing similar behavior). Thus, the multiscale model explicitly determines the microstructure throughout the fuel pellet.

The radial variation in void formation results in radial variation in thermal conductivity and temperature. The effect of void formation on thermal conductivity and the pellet temperature is demonstrated by comparing the results to an unirradiated pellet. The values of the thermal conductivity and the temperature at various radii for the irradiated and the pure, unirradiated pellets are shown in Fig. 6(b). Due to large voids in the center of the irradiated pellet, the thermal conductivity is significantly lower than that in the pure pellet. On the cooler outer edge, where only a few small voids have formed, the thermal conductivity is only slightly lower than that in the pure pellet. The low internal thermal conductivity reduces the transfer of heat to the pellet surface, and therefore the center temperature is 27 K hotter in the irradiated pellet than in the pure pellet. While quite simple due to the elementary models employed at both scales, these results reflect general behavior observed in fission reactors.

2.4 PRONGHORN

Pronghorn is a core simulator for Pebble-Bed Reactors (PBR), a type of Very High Temperature gas-cooled Reactors (VHTR) and models three distinct physical phenomena in a tightly coupled fashion: neutronics, fluid dynamics, and solid-state heat conduction. Currently, all physical phenomena are simplified in some way, and they reside on the same spatial mesh.

2.4.1 Governing equations

The following discussion summarizes the governing equations for this application. For a more complete discussion of the code and description of the physical models, see [4].

2.4.1.1 Fluid medium The flow in a PBR is represented as a porous media flow model as follows:

$$\frac{\partial \epsilon \rho_f}{\partial t} + \nabla \cdot \epsilon \rho_f \vec{u} = 0, \quad (2.10)$$

$$\epsilon \nabla P - \epsilon \rho_f \vec{g} + W \rho_f \vec{u} = 0, \quad (2.11)$$

$$\frac{\partial}{\partial t} [\epsilon \rho_f c_{pf} T_f] + \nabla \cdot (\epsilon \rho_f c_{pf} \vec{u} T_f) - \nabla \cdot \epsilon \kappa_f \nabla T_f + \alpha (T_f - T_s) = 0, \quad (2.12)$$

where ρ , \vec{u} , P , and T are density, velocity, pressure and temperature, respectively. Also, ϵ , \vec{g} , W , c_p , κ , and α are the porosity, gravity, friction factor, heat capacity, thermal conductivity and heat transfer coefficient. The subscripts, f and s , denote the fluid and solid medium. To close the system, an equation of state for an ideal gas is used,

$$P = \rho_f R T_f, \quad (2.13)$$

where R is the gas constant. (2.11) is solved for $\rho_f \vec{u}$ and then substituted into (2.10) to form the pressure Poisson equation,

$$\frac{1}{RT_f} \frac{\partial \epsilon P}{\partial t} - \nabla \cdot \frac{\epsilon^2}{W} \nabla P + \nabla \cdot \frac{\epsilon^2 \rho_f \vec{g}}{W} = 0. \quad (2.14)$$

The corresponding boundary conditions for the fluid medium are expressed as

$$\begin{aligned} P &= P_0, & \in \Gamma_O, \\ \vec{n} \cdot \left[-\frac{\epsilon}{W} \nabla P + \frac{\epsilon \rho_f \vec{g}}{W} \right] &= \vec{n} \cdot \rho_f \vec{u}_{in}, & \in \Gamma_I, \\ \vec{n} \cdot \left[-\frac{\epsilon}{W} \nabla P + \frac{\epsilon \rho_f \vec{g}}{W} \right] &= 0, & \in \Gamma_W, \end{aligned} \quad (2.15)$$

and

$$\begin{aligned} T_f &= T_0, & \in \Gamma_I, \\ \vec{n} \cdot [\epsilon \kappa_f \nabla T_f] &= 0, & \in \Gamma_{W,O}, \end{aligned} \quad (2.16)$$

for the pressure and thermal energy equation, respectively. Here, Γ_I , Γ_O , and Γ_W denote inlet, outlet and solid wall boundaries. Material properties, such as thermal conductivity, friction factor, and heat transfer coefficient, are computed using the KTA standard [33–35].

2.4.1.2 Solid medium The solid medium is represented by the following heat conduction equation,

$$\begin{aligned} \frac{\partial}{\partial t} [(1-\epsilon)\rho_s c_{ps} T_s] - \nabla \cdot \kappa_{s,\text{eff}} \nabla T_s + \alpha(T_s - T_f) - Q &= 0, \\ T_s &= T_0, & \in \Gamma_D, \\ \vec{n} \cdot \kappa_{s,\text{eff}} \nabla T_s &= 0, & \in \Gamma_A, \end{aligned} \quad (2.17)$$

where $\kappa_{s,\text{eff}}$ and Q are the effective thermal conductivity and heat source, respectively. Γ_D and Γ_A denote Dirichlet and adiabatic boundaries. The effective thermal conductivity is computed via the Zehner-Schlünder correlation discussed in [36], which can be represented as:

$$\kappa_{s,\text{eff}} = \kappa_s^r + \kappa_s^g + \kappa_s^c, \quad (2.18)$$

where κ_s^r , κ_s^g , and κ_s^c are the effective conductivities due to radiation between pebbles, conduction through gas media, and contact between pebbles, respectively. The detailed correlations for the thermal conductivity can be found in [36].

2.4.1.3 Neutronics The code employs a multigroup diffusion approximation for the neutronics calculation,

$$\frac{1}{v_g} \frac{\partial \phi_g}{\partial t} - \nabla \cdot D_g \nabla \phi_g + \Sigma_{Rg} \phi_g - (1 - \beta) \chi_g \sum_{g'} \nu \Sigma_{fg'} \phi_{g'} - \sum_{g', g' \neq g} \Sigma_s^{g' \rightarrow g} \phi_{g'} - \sum_k \lambda_k C_k = 0, \quad (2.19)$$

$$\frac{\partial C_k}{\partial t} + \lambda_k C_k - \sum_{g'} \beta_{k,g'} \nu \Sigma_{fg'} \phi_{g'} = 0, \quad (2.20)$$

where ϕ and C are the neutron flux and the delayed neutron precursor concentration. D , Σ_R , Σ_f , and Σ_s are the diffusion coefficient and the removal, fission and scattering cross-sections of prompt neutrons. v , β , χ , ν and λ are the prompt neutron speed, delayed neutron fraction, fission spectrum, average number of neutrons produced per fission event, and decay constant of delayed neutrons. The subscripts $g = 1, 2, \dots, G$, and $k = 1, 2, \dots, K$ are group indices of the multigroup neutron diffusion equations and precursor equations, respectively.

The following reflective and vacuum (2.21) boundary conditions are applied to close the system,

$$\begin{aligned} \vec{n} \cdot D_g \nabla \phi_g &= 0, & \in \Gamma_S, \\ \vec{n} \cdot D_g \nabla \phi_g + \frac{\phi}{2} &= 0, & \in \Gamma_V. \end{aligned} \quad (2.21)$$

2.4.2 Coupled transient benchmark

This section presents code-to-code comparisons for several transient PBMR400 benchmark problems [37, 38].

2.4.2.1 Reactivity insertions by control rod withdrawal (CRW) and ejection (CRE)

The first transient case is a total control rod withdrawal (CRW) transient, that corresponds to the TR5a case of the PBMR400 benchmark [37]. The control rod is withdrawn during the first 200 seconds, introducing a slow increase in the core power. During CRW, the core power increases to about 200% of steady state power. Fig. 7 compares the power profile of this transient. In this calculation, all the results match qualitatively, and two of the codes (MARS-GCR and TINTE) exhibit large oscillation in the solution due to the cusping effect. The cusping occurs when the mesh size is large in comparison to the movement of the control rod. The PRONGHORN results do not exhibit the cusping effect due to the refined mesh around the control rod. This calculation used second-order Lagrangian finite elements where $\Delta z = 6.25\text{cm}$. Since there are two quadrature (integration) points in z-direction per second-order Lagrangian element, this discretization can discern rod motion to an accuracy of approximately 3cm, which corresponds to a 3sec time interval in this transient. Here, a time step of $\Delta t = 2\text{sec}$ was also used. Given this time and spatial resolution, the problem is sufficiently resolved such that no significant

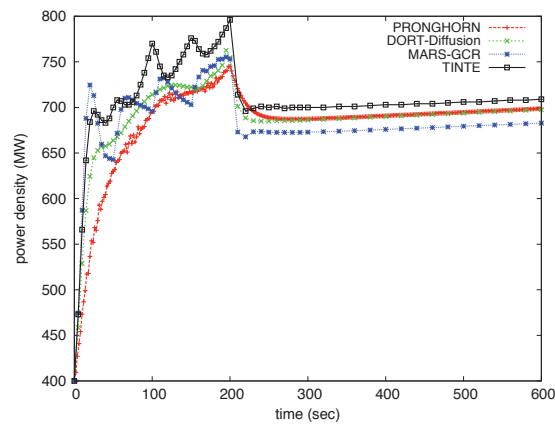


Figure 7: Comparison of power evolution in control rod withdrawal.

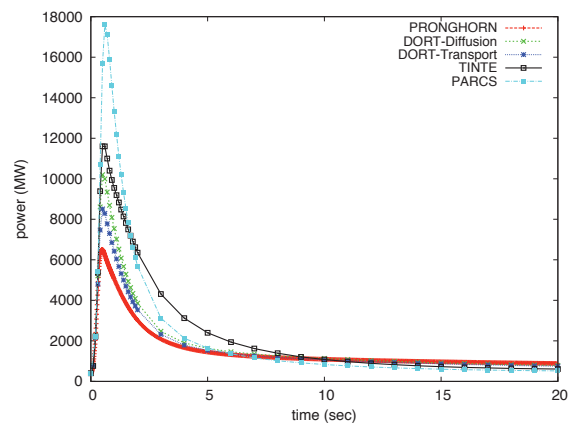


Figure 8: Comparison of power evolution in control rod ejection.

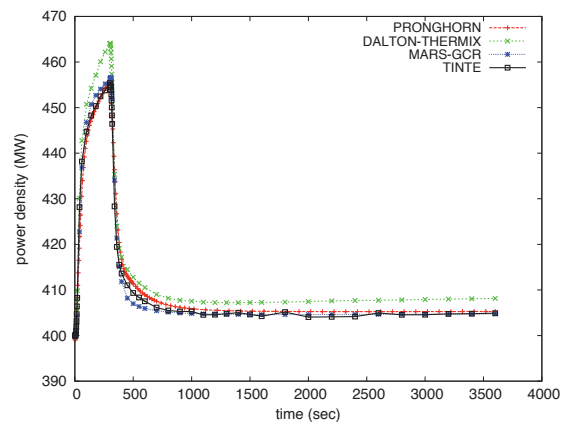


Figure 9: Comparison of power evolution in cold helium inlet transient.

cusping is seen. In this transient, a power peak occurs at $t = 200$ s. Due to being fully resolved, the PRONGHORN results show much less variation in the power peak ($< 10\%$ of a relative difference compared to the other participants).

The next transient is a total control rod ejection (CRE). The problem corresponds to the TR5b case of the PBMR400 benchmark [37]. In this transient, the control rod is ejected over a period of 0.1 second, which creates a super-prompt critical transient. Fig. 8 shows a comparison of the power profile of this transient. As seen in the figure, all the codes produced a power peak at the same time, and the decay ratio from the point of maximum power is quite similar. However, the maximum power at the peak shows a large variation between participants (300% difference). This difference is likely due to the different time dependent fuel kernel temperature models used in each code. Another possible cause of this difference is due to operator splitting issues. The JFNK approach in PRONGHORN tightly couples all the physics within a given time step. As discussed in Part I [1] and [4], an operator-split approach introduces a truncation error proportional to the time step employed. Moreover, in case of positive Doppler feedback, the computed power peak, in general, assumes a greater magnitude than the true power peak. These operator splitting errors alone might explain the difference in the maximum power calculated by the different participants in this transient.

2.4.2.2 Cold helium inlet The final PRONGHORN result is a calculation of a cold helium inlet transient. This problem corresponds to the TR6 case of the PBMR400 benchmark. In this transient, the inlet helium temperature is reduced by 50K linearly over the first 10 seconds of the transient event. At this point, the inlet temperature is held steady for the next 300 seconds, and then brought back to the original temperature. The cold helium introduces a small positive reactivity into the system. Fig. 9 compares the power profiles of this transient. As can be seen from the figure, all the codes produced very close power profiles, including the peak power, time of the peak, and the resulting steady state power. The maximum difference at the peak power is $< 3\%$, which was displayed by the DALTON-THERMIX code [39].

The final section of this paper transitions from nuclear energy applications to energy extraction and environmental analysis multiphysics applications.

2.5 FALCON and RAT: fluid dynamics and reactive transport in porous media

Problems involving coupled multiphysics processes associated with fluid dynamics and reactive transport in porous media are quite common. The final section of this paper describes two porous media simulation codes that employ the MOOSE framework, FALCON (*Fracturing And Liquid CONservation*) and RAT (*ReActive Transport*). These codes, while closely related in some aspects, are being developed for significantly different applications. The FALCON code is being designed to simulate geothermal reservoirs, and specifically enhanced geothermal systems, where multiphase fluid flow, energy transport, and deformation of the geologic media are strongly coupled. The RAT code is being

designed primarily to simulate single-phase fluid flow, reactive geochemistry, and the interactions between reactions and media properties. The sections below describe the governing equations for some simple applications of both the FALCON and RAT codes, and provide examples of their application.

2.5.1 FALCON: Fracturing And Liquid CONservation

Reliable reservoir performance predictions of enhanced geothermal reservoir systems require accurate and robust modeling of the coupled thermal-hydrological-mechanical processes. Conventionally, these types of problems are solved using operator splitting methods, usually by coupling a subsurface flow and heat transport simulator with a solid mechanics simulator via input files. One example of such an approach is presented by Rutquist *et al.* [40], where a widely used flow and heat transport simulator TOUGH2 [41] is coupled to the commercial rock mechanics simulator FLAC [42] via input files. During each time step, TOUGH2 and FLAC run sequentially with the output from one code as input to the other. Iterations between the codes during each step might be necessary if there is a strong dependence among processes and parameters. However, as discussed previously such operator splitting approaches are applicable only to *loosely coupled* problems. For most enhanced geothermal systems, fluid flow, heat transport, and rock deformation are typically strongly nonlinearly coupled.

An alternative approach is to solve the system of nonlinear partial differential equations that govern the system simultaneously using a fully coupled solution procedure. This approach obtains an approximate solution for all variables (fluid pressure, temperature and rock displacement fields) simultaneously, which leads to one large nonlinear algebraic system that is solved using a strongly convergent nonlinear solver.

2.5.1.1 Governing equations Mathematical models describing geothermal systems and geomechanics are common in the literature. Here we briefly summarize the governing equations and constitutive relationships for geothermal systems (see [43–45] for more detail) and for geomechanics (see [46]). We will focus discussion on the unique aspects of coupling the governing equations for fully coupled implicit solutions.

The following presents the conservation equations for mass, momentum, and energy. The mass balance for the fluid may be written as:

$$\frac{\partial(n\rho_w)}{\partial t} + \nabla \cdot (\rho_w \mathbf{q}) - \dot{q}_w = 0, \quad (2.22)$$

where \mathbf{q} is the flux (Darcy Velocity) vector, ρ_w is the water density, and n is the porosity of the reservoir.

When considering the momentum balance of the system, we assume that Darcy's Law is valid and that the momentum balance for the water may be represented as

$$\mathbf{q} = -\frac{k}{\mu_w} \cdot (\nabla p_w - \rho_w g \nabla z), \quad (2.23)$$

where k is the intrinsic permeability of the reservoir, μ_w is the viscosity of the water, g is the acceleration due to gravity, and ∇z is a vector of components $[0,0,1]$ when gravity is taken to be aligned in the negative vertical direction.

The energy balance in the system can be described as

$$\frac{\partial [n\rho_w h_w]}{\partial t} + \nabla \cdot (\rho_w h_w \mathbf{q}) + \nabla \cdot \lambda_{cw} + \nabla \cdot \lambda_{dw} - \frac{\partial (\phi p_w)}{\partial t} - \mathbf{q} \cdot \nabla p_w - q'_w h'_w = 0 \quad (2.24)$$

for the fluid phase and

$$\frac{\partial [(1-n)\rho_r h_r]}{\partial t} + \nabla \cdot \lambda_{cr} = 0 \quad (2.25)$$

for the reservoir rock matrix, where h is the specific enthalpy, λ_c is the heat conduction vector, and λ_d is the dispersion vector. Accented terms represent sources and/or sinks in the preceding equations.

Combining (2.22) and (2.23) yields the following for single-phase flow of water in a deformable, compressible geologic medium

$$\frac{\partial (\phi c_f p)}{\partial t} - \nabla \cdot \left[\frac{k\rho_w}{\mu_w} \cdot (\nabla p_w - \rho_w g \nabla z) \right] - q'_w = 0. \quad (2.26)$$

For a simplified demonstration of the simulation code, thermal equilibrium was assumed between fluid and rock when combining (2.26) with (2.24). The *Boussinesq Approximation* [47] was also used to describe the transport of heat in the system, to arrive at the following heat transport equation:

$$[n\rho_w c_w + ((1-n)\rho_r c_r)] \frac{\partial T}{\partial t} - \nabla \cdot (K_m \nabla T) + \rho_w c_w \mathbf{u}_w \cdot \nabla T = 0, \quad (2.27)$$

where c_w and c_r are the specific heat capacities of the water and rock phases, respectively, and K_m is the medium average thermal conductivity.

Geomechanics of the system is described as follows [46]

$$\rho \frac{\partial^2 \mathbf{u}}{\partial t^2} - \nabla \cdot \sigma - \rho \vec{g} - \alpha \nabla p - \beta K \nabla T = 0, \quad (2.28)$$

where \mathbf{u} is the displacement vector, α is the Biot effective stress coefficient and β is the thermal expansion coefficient. (2.28) provides stress equilibrium for a coupled thermal-hydro-mechanical problem.

2.5.1.2 Constitutive relationships For the simplified single-phase system, constitutive relations are used to describe the fluid density and viscosity dependence on the temperature.

The density dependence on temperature is described by Graf [48]

$$\rho_w = 1000 \cdot \left[1 - \frac{(T - 3.9863)^2}{508929.2} \cdot \frac{T + 288.9414}{T + 68.12963} \right], \quad (2.29)$$

where T is the temperature in degrees Celsius and ρ_w is in dimensions of kg/m^3 . Fluid viscosity is represented by the following set of equations, also presented by Graf [48]

$$\mu_w = \begin{cases} 1.787 \times 10^{-3} \cdot \exp((-0.03288 + 1.962 \times 10^{-4} \cdot T) \cdot T), & \text{for } 0^\circ\text{C} \leq T \leq 40^\circ\text{C}, \\ 10^{-3} \cdot (1 + 0.015512 \cdot (T - 20))^{-1.572}, & \text{for } 40^\circ\text{C} < T \leq 100^\circ\text{C}, \\ (0.2414 \times 10^{(247.8/(T+133.15))}) \cdot 10^{-4}, & \text{for } 100^\circ\text{C} < T \leq 300^\circ\text{C}, \end{cases} \quad (2.30)$$

with μ_w having dimensions of $\text{Pa} \cdot \text{sec}$.

2.5.1.3 Results As an example of FALCON's capabilities, consider modeling of a coupled thermoporoelastic problem in the vicinity of injection well to simulate the injection of cold water into an initially hot reservoir. Initially, consider only fluid-rock interaction and ignore the thermal-induced rock deformation effect (a classical poroelasticity problem) and follow with a fully coupled thermo-hydro-mechanical problem on the same domain. Both lateral and bottom boundaries are confined (with prescribed zero lateral displacement). For both problems water is injected via an injection well in the middle of the domain at a constant rate.

Fig. 10 (left) shows the simulation results of the final 3D pressure and rock displacement fields. The simulation results clearly show the coupling of fluid injection and rock deformation and are qualitatively reasonable. The rock bulging out across the top surface due to the lateral confinement boundary condition used in this simulation. Note that the vertical displacement has been greatly exaggerated to highlight the bulging effect. The actual vertical and lateral displacements are in reality very small. The lateral displacement field indicates that the rock is "pushed" away from the injection well, also clear evidence of fluid-rock interaction. Also notice that in this simulation, only fluid to rock displacement is modeled for simplicity. The effect of rock deformation on fluid flow can be readily incorporated into the simulation.

A more complex problem is to add heat transport and couple all three processes (fluid flow, heat transport, and rock deformation due to both fluid injection and thermal-induced stress) together by solving all three governing equations (2.26)-(2.28) simultaneously. Fig. 10 (right) shows the simulation results for such a problem. In this simulation, cold water at 20°C is injected into the reservoir that is initially at a temperature of 100°C , which leads to decreasing reservoir temperature. Therefore the rock near the wellbore tends to shrink toward the injection well due to cooling, a processes similar to land subsidence due to excessive groundwater pumping. A close comparison of the magnitudes of the vertical displacement on Fig. 10 indicates that in this particular example, the deformation of rock due to reservoir cooling is far more significant that due to injection of water. Thus the rock near the wellbore is under tension. One immediate application

of the simulation results is to evaluate the stress state near the wellbore and assess the potential of rock failure.

The second example examines a case of density driven free thermal convection, similar to that detailed by Elder [49], in which a water saturated homogeneous isotropic medium is heated from the bottom causing a large density change ($>5\%$) and leads to unstable flow. This example was chosen to demonstrate FALCON's capabilities for fully coupling the fluid flow and heat transport equations along with the temperature-dependent constitutive relations for fluid density and viscosity, as well as adaptive mesh refinement. The simulation domain and boundary condition locations chosen for the problem follows those detailed by Oldenberg and Pruess [50], using symmetry about the midpoint of the x -axis of the Elder problem, reducing the domain size to 300 meters by 150 meters. Initial conditions chosen for the problem are a hydrostatic pressure distribution and a uniform 12°C over the entire domain. The bottom left ($x=0$ to 150m) boundary condition imposed at startup applies a constant temperature of 20°C , and initiates a density driven instability into the system. Relevant material properties used in the simulation are an intrinsic permeability of $1 \times 10^{-10} \text{ m}^2$, porosity of 0.40, rock specific heat of $920.0 \text{ J/kg}^\circ\text{C}$, and a rock density of $2,500 \text{ kg/m}^3$. Fluid density and viscosity are initialized at values provided from the constitutive relations provided above. The problem was specifically parameterized to be convection dominated and have a large Rayleigh number, testing the stability and efficacy of the code. Oldenberg and Pruess [50] showed that the results of this problem are strongly grid dependent, with a relatively coarse grid returning [upward] flows concentrated along the axis of symmetry in their simulations. When a finer grid was used an area of downwelling was predicted along the axis of symmetry.

For this example, three simulation cases were tested with FALCON, focusing on (1) a static fine mesh scenario and (2) initially coarse mesh scenarios with adaptive mesh refinement. The cases were 1) a uniform 1m by 1m mesh, 2) an initially uniform 10m by 10m mesh with aggressive adaptive mesh refinement, and 3) an initially uniform 10m by 10m mesh with conservative adaptive mesh refinement. Shown on Fig. 11 is the temperature distribution after twenty years of simulated time. The red color represents a temperature of 20°C , whereas the blue color represents 12°C .

As can be seen on Fig. 11, the results for the two adaptive mesh simulations provide similar results, whereas there is a difference when compared to the static fine mesh simulation. Frolkovic and DeSchepper [51], when comparing the results of fine grid simulations and adaptive mesh applications, reported adaptive mesh results identical to those obtained with an extremely fine mesh. While our fine mesh test case does not directly compare with those of Frolkovic and DeSchepper [51], examination and comparison of the simulation case results are illustrative of the potential gains in computational capability obtained with FALCON. The first simulation case using a uniform 1m by 1m grid (45,000 grid blocks), shown in the top frame on Fig. 11, predicted a large central upwelling zone and three additional upwelling fingers. The 20-year simulation required approximately 2,100 seconds for the calculations using a parallel scheme with 8 proces-

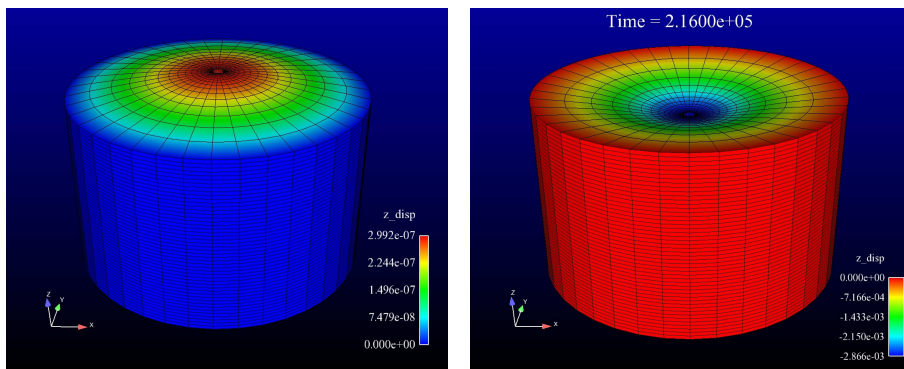


Figure 10: Simulated steady state vertical displacement field results for the poroelastic (left) and thermoporoelastic (right) problems. Note that displacement fields are exaggerated for visual impact.

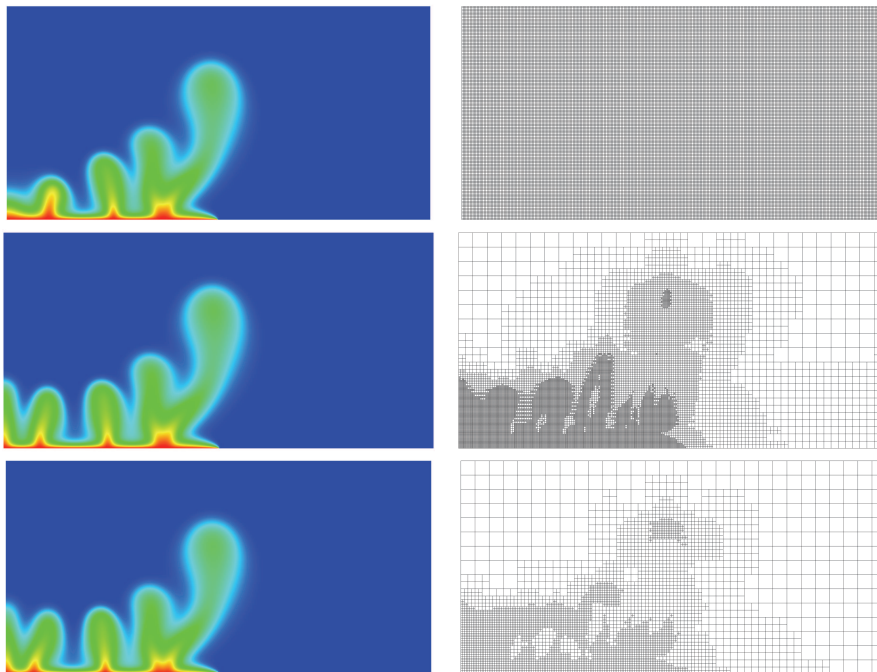


Figure 11: Simulated temperature distribution (left) and corresponding computational mesh (right) for unstable thermal convection using a static mesh (top), aggressive adaptive mesh (middle), and conservative adaptive mesh (bottom).

sors and a uniform timestep of 10 days. The second and third cases, both using an initial 10m by 10m mesh and adaptive mesh refinement, produced very similar results. For the second (aggressive adaptive mesh refinement) case, the mesh refinement was allowed to reduce the grid cells to 0.15m by 0.15m, and forced the refined areas to persist over a large area of the simulated domain. As the mesh evolved over the duration of the simulation, the simulation time actually suffered when compared to the uniform mesh case, requiring

Table 1: Summary the 2-Dimensional simulations.

Simulation Case	Mesh Type	Mesh Maximum Size (<i>m</i>)	Mesh Minimum Size (<i>m</i>)	Execution Time (<i>s</i>)
1	Uniform	1×1	1×1	2,100
2	Adaptive	10×10	0.15×0.15	4,077
3	Adaptive	10×10	1.25×1.25	434

a total of 4,077 seconds to simulate 20 years of convection. The aggressive mesh refinement resulted in the existence of 37,047 grid cells at the conclusion of the simulation. The third test case produced similar results as the second case (see Fig. 11), but with much less computational burden. Allowing the grid only to refine only to a uniform 1.25m cell size, and relaxing the grid after perturbations passed by, reduced the computational time to 434 seconds to complete the simulation with 5,826 grid cells existing at the conclusion of the run. A summary of these results is shown in Table 1.

While our results are preliminary and qualitative in nature, they are very promising. Significant reductions in computational time were achieved using adaptive meshing capabilities. Questions remain regarding quantification of the simulation results and predicted temperature distribution. Work is currently ongoing to quantify the solution of the problems and benchmark the code performance against existing simulators such as TOUGH2 [41].

2.5.2 RAT: ReActive Transport

Reactive transport is a multiphysics problem in which physical and chemical processes of fluid flow, solute transport, and reactions are coupled. Three major solution approaches are considered for reactive transport modeling in terms of coupling between transport and reactions: a global implicit (fully-coupled) method, a sequential iteration approach (loosely-coupled), and a sequential non-iteration approach (operator-splitting) [52, 53]. Currently widely used subsurface reactive transport codes (*e.g.*, TOUGHREACT [54] and STOMP [55,56]) adopt the operator-splitting approach because it is the simplest approach to implement and, more importantly, requires the least computational resources. However, such an approach is not applicable to reactive transport problems that involve strong mineral-solution interactions, and where reactions are tightly coupled with fluid flow and transport of reactants. Such situations are quite common, and are associated with most subsurface environmental remediation efforts where chemical conditions are typically far from equilibrium. Today, given the advances in computational hardware and algorithms for solving system of nonlinear equations, we are now able to implement the fully-coupled, fully implicit approach for modeling reactive transport in porous media. Hence, a new fully-coupled, fully-implicit reactive transport simulator, RAT, was developed using the MOOSE platform.

2.5.2.1 Mathematical formulation RAT currently describes single phase, incompressible flow in porous medium as Darcy flow:

$$S_s \frac{\partial h}{\partial t} = \nabla(\mathbf{K} \cdot \nabla h) + q_w, \quad (2.31)$$

where h is the hydraulic head, S_s denotes the specific storage of the aquifer, \mathbf{K} is hydraulic conductivity tensor, and q_w is a volumetric flux per unit volume representing sources and/or sinks of water.

The governing equation describing the fate and transport of the dissolved nonreactive solute can be written as follows [57]:

$$\frac{\partial(\theta C)}{\partial t} = \nabla(\theta \mathbf{D} \cdot \nabla C) - \nabla(\theta \mathbf{V} \cdot C) + q_w C_s, \quad (2.32)$$

where θ is the porosity of the medium, C is concentration of dissolved solute, \mathbf{D} represents hydrodynamic dispersion coefficient tensor, \mathbf{V} is the linear pore water velocity calculated from the flow equation, q_w denotes the volumetric flow rate per unit volume of aquifer representing fluid sources (positive) and sinks (negative), and C_s is the concentration of species in source or sink water.

Geochemical reactive systems in subsurface environments are generally mixed equilibrium-kinetic systems. When aqueous reactions are constrained by local equilibrium, mass transport equations are not all independent [58]. Thus, we select a subset of N_c species, often called component species to describe the system. However, when there are aqueous phase reactions that are not sufficiently fast for a given time scale of interest that they reach equilibrium, we will also need kinetic species to fully describe the system. The remaining species are called equilibrium species that is written in terms of a nonlinear combination of one or more component and/or kinetic species. As a result, the total number of transport equations is reduced to only the number of component and kinetic species. A general form of the transport equation for component species becomes [56]:

$$\frac{\partial C_{tc,j}}{\partial t} = \nabla \left[\theta \mathbf{D} (\nabla C_{tc,j}^m) \right] - \nabla (\theta \mathbf{V} C_{tc,j}^m) - \sum_{i=1}^{N_{tc,j}^s} q_i + \sum_{k=1}^{N_{tc,j}^r} R_{tc,j,k}, \quad (2.33)$$

in which $C_{tc,j}$ is the total concentration of component species j , $C_{tc,j}^m$ is the total dissolved mobile concentration of component species j (*i.e.*, mobile fraction of a primary species), q_i is the i^{th} source/sink rate for all $N_{tc,j}^s$ individual species involved in component species j , $R_{tc,j,k}$ is the rate of concentration changes in the j^{th} component associated with the k^{th} kinetic reaction that either generates or consumes this component species, and $N_{tc,j}^r$ is the total number of kinetic reactions associated with the component species j .

The transport equation for kinetic species takes a similar form as the component species [56]:

$$\frac{\partial C_{tk,j}}{\partial t} = \nabla \left[\theta \mathbf{D} (\nabla C_{tk,j}^m) \right] - \nabla (\theta \mathbf{V} C_{tk,j}^m) - \sum_{i=1}^{N_{tk,j}^s} q_i + \sum_{k=1}^{N_{tk,j}^r} R_{tk,j,k}, \quad (2.34)$$

in which $C_{tk,j}$ is the total concentration of kinetic species j , $C_{tk,j}^m$ is the total mobile concentration of kinetic species j , q_i is the i^{th} source/sink rate for all $N_{tk,j}^s$ individual species involved in kinetic species j , $R_{tk,j,k}$ is the rate of concentration change in the j^{th} kinetic species associated with the k^{th} kinetic reaction, and $N_{tk,j}^r$ is the total number of kinetic reactions associated with the kinetic species j .

For the j^{th} component species, the total concentration is expressed as a stoichiometrically weighted summation of all individual species that are involved [53]:

$$C_{tc,j} = C_j + \sum_{N_{tc,j-1}^s} (a_i C_i), \quad \text{for } j=1, N_{cn}, \quad (2.35)$$

where N_{cn} is the number of component species in the system, C_j and C_i refer to the concentration of the component and equilibrium species respectively, and a_i is stoichiometric coefficient for $N_{tc,j}^s - 1$ equilibrium species involved in the j^{th} component species. Similarly for a kinetic species, the total concentration can also be expressed generally as:

$$C_{tk,j} = C_j + \sum_{N_{tk,j-1}^s} (b_i C_i), \quad \text{for } j=1, N_{kn}, \quad (2.36)$$

where N_{kn} is the number of kinetic species in the system, C_j refers to the concentration of the kinetic species, b_i is stoichiometric coefficient for $N_{tk,j}^s - 1$ equilibrium species involved in the j^{th} kinetic species, and C_i is the concentration of these species.

By using the mass action law, equilibrium species concentrations are related to component and kinetic species concentrations through equilibrium constants [56]:

$$(C_i) = K_{eq,i} \prod_{N_{c/k,i}} (C_j)^{e_j}, \quad \text{for } i=1, N_{eq}, \quad (2.37)$$

where N_{eq} is the number of equilibrium reactions (and also the number of the equilibrium secondary species), (C_i) is the activity of equilibrium species i , $K_{eq,i}$ is the equilibrium constant of the i^{th} equilibrium reaction, $N_{c/k,i}$ is the total number of component and/or kinetic species that form the i^{th} equilibrium species, (C_j) is the activity of these component and/or kinetic species, and e_j is the stoichiometric coefficient for them.

The rate of change in concentration of component and kinetic species j due to kinetic reactions is a weighted sum of kinetic rates of these reactions:

$$\sum_{N_{tc/tk,j}^r} R_{tc/tk,j,k} = \sum_{N_{tc/tk,j}^r} (c_k R_k), \quad (2.38)$$

where $N_{tc/tk,j}^r$ is the number of kinetic reaction associated with the j^{th} component or kinetic species, c_k is the reaction-rate coefficient that is related to the stoichiometric coefficient for the k^{th} kinetic reaction, and R_k is the reaction rate of the k^{th} reaction. There are a variety of kinetic rate expressions one may apply depending on the specific reaction and the conditions. See [56,59] for examples of different kinetic rate laws.

By substituting the expressions (2.35), (2.36), (2.37), and (2.38) into the component and kinetic species transport equations (2.33) and (2.34), we have a system of nonlinear equations that fully describes the reactive transport system. Solving this system using RAT produces a fully-coupled solution of the reactive transport problem.

2.5.2.2 Example application We applied RAT to simulate calcite precipitation driven by urea hydrolysis that is catalyzed by enzyme urease. This process has been studied as a promising *in situ* remediation approach to immobilize metal contaminants and radionuclides in groundwater [60–62]. Metal contaminants can either coprecipitate with calcite or be isolated by calcite precipitates that reduce permeability. Laboratory experiments and numerical simulations using RAT are being conducted to advance the scientific understanding of this potential remediation approach. The physical experiments consist of porous media (silica gel) columns with zones of immobilized extracellular urease, through which solutions containing urea and calcium are passed (Fig. 12); the experiments are conducted at Idaho National Laboratory (INL) under the auspices of the DOE Office of Science Subsurface Biogeochemical Research program. The purposes of the modeling are to help develop hypotheses and guide the design of the experiments through pre-experimental simulations, to aid data interpretation after the experiments, and to support the understanding of the nonlinear coupling effects between various processes.

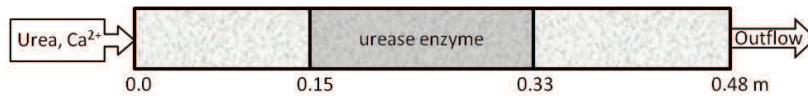


Figure 12: The schematic diagram of configuration of the flow column in the experiment.

The reactions that are identified to represent this system include 8 aqueous equilibrium reactions, one aqueous kinetic reaction, and a kinetic solid precipitation reaction (Table 2). The rate expressions for the two kinetic reactions of calcium carbonate precipitation (R_{10} in Table 2) and urea hydrolysis (R_9 in Table 2) are shown here, based on the standard transition state theory rate law from [63] and the modified Michaelis-Menten rate law from [64], respectively:

$$R_{precip_dissl} = Ak \left[1 - \frac{Q}{K_{eq}} \right], \quad (2.39)$$

where

$$k = k_{ref} \cdot e^{\frac{-E_a}{R} \left(\frac{1}{T} - \frac{1}{T_{ref}} \right)}, \quad (2.40)$$

$$R_{ureolysis} = C_{urease} \cdot \frac{k_{ref} \cdot e^{\frac{-E_a}{R} \left(\frac{1}{T} - \frac{1}{T_{ref}} \right)} \cdot C_{urea}}{(K_M + C_{urea}) \cdot \left(1 + \frac{C_{NH_4^+}^{total}}{K_P} \right) \cdot \left(1 + \frac{C_{H^+}}{K_{ES,1}} + \frac{K_{ES,2}}{C_{H^+}} \right)}. \quad (2.41)$$

Table 2: The reaction network identified to simulate ureolytically driven calcium carbonate precipitation system (equilibrium constants are from the EQ3/6 data base [65]).

Aqueous Equilibrium Reactions	$K_{eq}(10^x)$	Kinetic Reactions
(R ₁) $CO_2(aq) \Leftrightarrow H^+ + HCO_3^-$	-6.341	(R ₉) $Urea \xrightleftharpoons{Urease} 2NH_4^+ + HCO_3^- + OH^-$
(R ₂) $CO_3^{2-} \Leftrightarrow -H^+ + HCO_3^-$	10.325	(R ₁₀) $Ca^{2+} + HCO_3^- \Leftrightarrow H^+ + CaCO_3(s)$
(R ₃) $CaCO_3(aq) \Leftrightarrow Ca^{2+} + HCO_3^- - H^+$	7.009	
(R ₄) $CaHCO_3^+ \Leftrightarrow Ca^{2+} + HCO_3^-$	-1.043	
(R ₅) $CaOH^+ \Leftrightarrow Ca^{2+} - H^+$	12.85	
(R ₆) $NH_3(aq) \Leftrightarrow NH_4^+ - H^+$	9.492	
(R ₇) $OH^- \Leftrightarrow -H^+$	13.991	
(R ₈) $\overline{SiO_2-OH} \Leftrightarrow \overline{SiO_2} - H^+$	9.5	

Table 3: Kinetics for Calcite Precipitation and Urea Hydrolysis, * value from [66], ** value from [56], *** values from [64] except for K_M and k_{ref} values that are measured by Karen Wright and Yoshiko Fujita at INL.

Calcite Precipitation Kinetics					
k_{ref}^*	A^{**}	E_a	T_{ref}	R	$\log_{10} K_{eq}$
6.456×10^{-9} mol/m ² s	4.61×10^{-4} m ² /L	1.5×10^4 cal/mol	298.15 K	8.314 J/mol K	1.8487

Urea Hydrolysis Kinetics***							
K_M	K_P	E_a	k_{ref}	T_{ref}	$K_{ES,1}$	$K_{ES,2}$	C_{urease}
6.99×10^{-3} mol/L	1.22×10^{-2} mol/L	8431.26 cal/mol	2.72×10^2 mol/mol s	298.15 K	7.57×10^{-7} mol/L	1.27×10^{-8} mol/L	2.083×10^{-7} mol/L

The parameter values used are listed in Table 3.

Ca^{2+} , H^+ , HCO_3^- , NH_4^+ , and urea were selected as component and kinetic species that have transport equations; all the equilibrium species involved in component and kinetic species are substituted into these equations by their mass action expressions. This set of fully-coupled nonlinear equations is then solved using RAT in a fully-implicit manner.

Fig. 13 shows the profiles of concentrations for major species of H^+ , urea, and NH_4^+ at the end of one pore volume, and comparisons to the measured concentration profiles (unpublished data obtained by Don Fox and George Redden at INL). The simulator was able to capture the trends in the experimental data although an offset in the values was observed which implied that the enzyme might have been mobilized and thus transported further downstream along the column over the course of the experiment. More detailed studies are being conducted at INL to investigate this hypothesis. The experimental data indicated that as urea hydrolysis occurred, pH rose in the column; although the reactivity of the silica gel with the hydroxide ion buffered this increase. Urea hy-

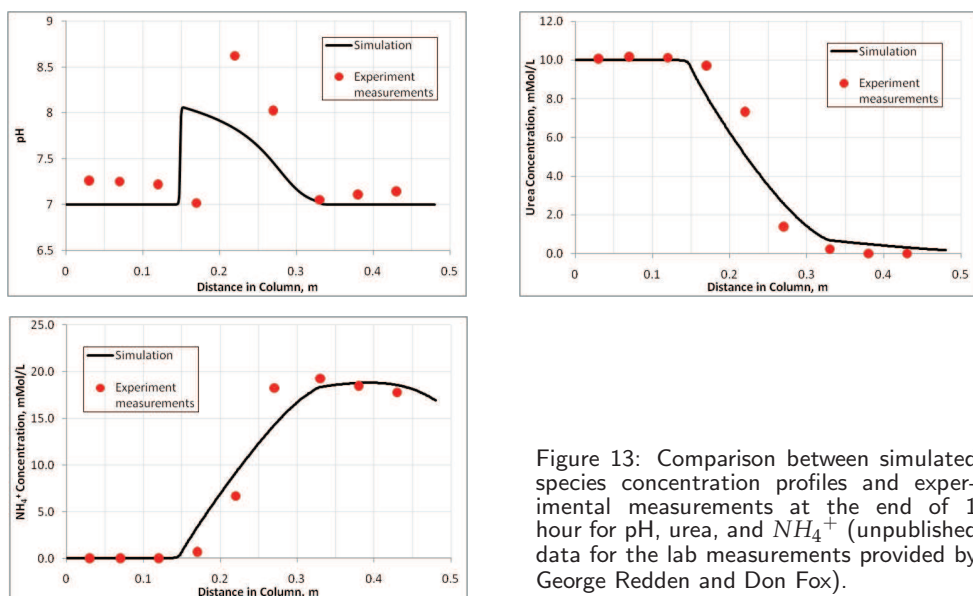


Figure 13: Comparison between simulated species concentration profiles and experimental measurements at the end of 1 hour for pH, urea, and NH_4^+ (unpublished data for the lab measurements provided by George Redden and Don Fox).

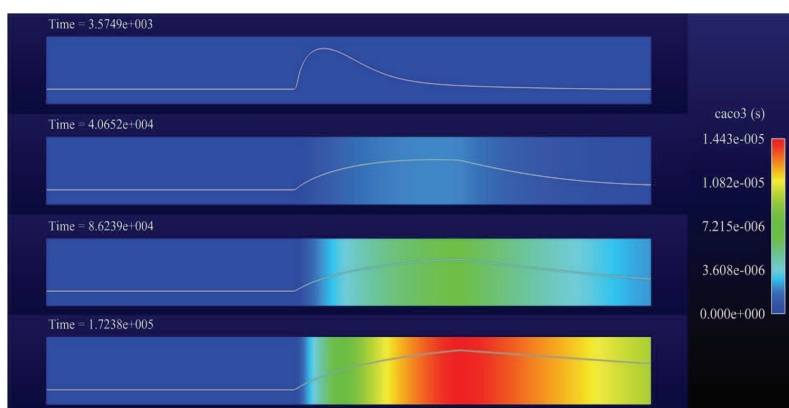


Figure 14: Simulation of temporal and spatial distribution of mineral precipitates, the color shows the increase in the amount of precipitates, and the solid lines show the distribution of the precipitates at different times.

drolyzed at a fairly high rate to generate a steep slope in the concentration profile over the enzyme zone; correspondingly, the concentration of product ammonium ion showed a sharp rise through the zone as well.

We also simulated the temporal and spatial distribution of the calcium carbonate precipitation (Fig. 14). The simulations predicted that the precipitation would start in the upstream part of the enzyme zone and migrate downstream to accumulate the majority of the precipitated solids towards the end of the enzyme zone. Consistent with the predicted outcome, the deconstruction of the column at the conclusion of the experiment indicated that the calcite was precipitated largely within the urease zone, with greater

precipitate deposited in the downstream portion of the zone. However, visual observations of the precipitate formation during the course of the experiment suggested the contrary in the time course of precipitation events in that the precipitation began to form toward the downstream end of the enzyme zone, and migrated to the front portion of the zone as the experiment progressed. The discrepancy between the simulation prediction and the experiment observations in the temporal variation of the precipitation distribution has led to the reevaluation of the assumptions and hypotheses made prior to the experiment. This is an example of the utility of RAT for interpretation of the complex behavior of the systems characterized by nonlinear process coupling.

3 Conclusions

Part II provided an overview of the MOOSE multiphysics framework and several applications based on it designed for engineering analysis. BISON is a multiscale multiphysics application for reactor fuel performance, PRONGHORN is designed for analysis of gas cooled pebble-bed reactors, FALCON for analysis of geothermal reservoirs, and RAT for single phase flow and reactive geochemistry.

MOOSE and its applications are based on a preconditioned Jacobian-free Newton Krylov (JFNK) method as it supports a general and straightforward software design pattern that allows rapid development of complex engineering analysis applications. As development on MOOSE started in 2008; the results presented in Part II demonstrate that this rapid development advantage is significant. Secondly, JFNK is a very robust solution algorithm for monolithic solution of multiphysics problems [67–69]. These features and results demonstrate a new paradigm in the area of multiphysics algorithm and software development for nuclear, energy, and environmental science applications.

Acknowledgments

The submitted manuscript has been authored by a contractor of the U.S. Government under Contract No. DE-AC07-05ID14517 (INL/JOU-10-20006). Accordingly, the U.S. Government retains a non-exclusive, royalty-free license to publish or reproduce the published form of this contribution, or allow others to do so, for U.S. Government purposes.

References

- [1] D. Gaston, L. Guo, G. Hansen, H. Huang, R. Johnson, D. Knoll, C. Newman, H. Park, R. Podgorney, M. Tonks, R. Williamson, Parallel algorithms and software for nuclear, energy, and environmental applications. Part I: Multiphysics algorithms, Commun. Comput. Phys. 12 (2012) 807–833.
- [2] D. Gaston, C. Newman, G. Hansen, D. Lebrun-Grandié, MOOSE: A parallel computational framework for coupled systems of nonlinear equations, Nucl. Engrg. Design 239 (2009) 1768–1778.

- [3] C. Newman, G. Hansen, D. Gaston, Three dimensional coupled simulation of thermomechanics, heat, and oxygen diffusion in UO₂ nuclear fuel rods, *Journal of Nuclear Materials* 392 (2009) 6–15.
- [4] H. Park, D. A. Knoll, D. R. Gaston, R. C. Martineau, Tightly coupled multiphysics algorithms for pebble bed reactors, *Nuclear Science and Engineering* 166 (2) (2010) 118–133.
- [5] B. S. Kirk, J. W. Peterson, R. H. Stogner, G. F. Carey, libMesh: a C++ library for parallel adaptive mesh refinement/coarsening simulations, *Eng Comput-Germany* 22 (3-4) (2006) 237–254.
- [6] S. Balay, W. D. Gropp, L. C. McInnes, B. F. Smith, Efficient management of parallelism in object oriented numerical software libraries, in: E. Arge, A. M. Bruaset, H. P. Langtangen (Eds.), *Modern Software Tools in Scientific Computing*, Birkhäuser Press, 1997, pp. 163–202.
- [7] M. Heroux, et al., Trilinos: an object-oriented software framework for the solution of large-scale, complex multi-physics engineering and scientific problems, <http://trilinos.sandia.gov> (2008).
- [8] R. D. Falgout, U. M. Yang, HYPRE: A library of high performance preconditioners, in: *International Conference on Computational Science* (3), 2002, pp. 632–641.
- [9] D. Braess, *Finite Elements: Theory, Fast Solvers, and Applications in Solid Mechanics*, Cambridge University Press, Cambridge, 2001.
- [10] S. C. Brenner, L. R. Scott, *The Mathematical Theory of Finite Element Methods*, Springer, New York, Berlin, Heidelberg, 2002.
- [11] U. M. Ascher, L. R. Petzold, *Computer Methods for Ordinary Differential Equations and Differential–Algebraic Equations*, SIAM, Philadelphia, PA, 1998.
- [12] I. Babuška, M. Suri, The p and $h-p$ versions of the finite element method, basic principles and properties, *SIAM Rev.* 36 (1994) 578–632.
- [13] G. F. Carey, *Computational Grids: Generation, Adaptation, and Solution Strategies*, Taylor & Francis, Washington, DC, 1997.
- [14] D. W. Kelly, J. P. De SR Gago, O. C. Zienkiewicz, I. Babuska, A posteriori error analysis and adaptive processes in the finite element method: Part I-error analysis, *Internat. J. Numer. Methods Engrg.* 19 (11).
- [15] M. Ainsworth, J. T. Oden, *A Posteriori Error Estimation in Finite Element Analysis*, Wiley Interscience, 2000.
- [16] J. K. Fink, Thermophysical properties of uranium dioxide, *J. Nucl. Materials* 279 (1) (2000) 1–18.
- [17] P. G. Lucuta, H. J. Matzke, I. J. Hastings, A pragmatic approach to modelling thermal conductivity of irradiated UO₂ fuel: review and recommendations, *Journal of Nuclear Materials* 232 (1996) 166–180.
- [18] G. K. Miller, D. A. Petti, J. T. Maki, D. L. Knudsen, PARFUME theory and model basis report, Tech. Rep. INL/EXT-08-14497, Idaho National Laboratory (2009).
- [19] C. M. Allison, et al., SCDAP/RELAP5/MOD3.1 code manual volume IV: MATPRO, Tech. Rep. NUREG/CR-6150, Idaho National Laboratory (1993).
- [20] Y. Rashid, R. Dunham, R. Montgomery, Fuel analysis and licensing code: FALCON MOD01, Tech. Rep. EPRI 1011308, Electric Power Research Institute (Dec. 2004).
- [21] K. Forsberg, A. R. Massih, Diffusion theory of fission gas migration in irradiated nuclear fuel UO₂, *Journal of Nuclear Materials* 135 (2-3) (1985) 140–148.
- [22] A. Denis, R. Piotrkowski, Simulation of isothermal fission gas release, *Journal of Nuclear Materials* 229 (1996) 149–154.
- [23] G. Hansen, R. Martineau, C. Newman, D. Gaston, Framework for simulation of pellet

- cladding thermal interaction (PCTI) for fuel performance calculations, in: American Nuclear Society 2009 International Conference on Advances in Mathematics, Computational Methods, and Reactor Physics, Saratoga Springs, NY, 2009.
- [24] G. Hansen, A Jacobian-free Newton Krylov method for mortar-discretized thermomechanical contact problems, *J. Comput. Phys.* 230 (2011) 6546–6562.
- [25] R. L. Williamson, C. K. Newman, Simulation of TRISO fuel using the BISON fuel performance code: Initial feasibility study, Tech. Rep. INL/INT-09-17415, Idaho National Laboratory (Dec. 2009).
- [26] C. M. Allison, G. A. Berna, R. Chambers, E. W. Coryell, K. L. Davis, D. L. Hagrman, D. T. Hagrman, N. L. Hampton, J. K. Hohorst, R. E. Mason, M. L. McComas, K. A. McNeil, R. L. Miller, C. S. Olsen, G. A. Reymann, L. J. Siefken, SCDAP/RELAP5/MOD3.1 code manual, volume IV: MATPRO—A library of materials properties for light-water-reactor accident analysis, Tech. rep., NUREG/CR-6150, EGG-2720 (1993).
- [27] V. Tikare, E. A. Holm, Simulation of grain growth and pore migration in a thermal gradient, *J. Am. Ceram. Soc.* 81 (3) (1998) 480–4.
- [28] J. Y. Oh, Y. H. Koo, B. H. Lee, Simulation of high burnup structure in UO_2 using Potts model, *Nucl. Eng. Technol.* 41 (8) (2009) 1109–14.
- [29] S. K. Rokkam, A. El-Azab, P. C. Millett, D. Wolf, Phase field modeling of void nucleation and growth in irradiated metals, *Modelling Simul. Mater. Sci. Eng.* 17 (2009) 064002.
- [30] P. C. Millett, D. Wolf, T. D. Desai, S. Rokkam, A. El-Azab, Phase-field simulation of thermal conductivity in porous polycrystalline microstructures, *Journal of Applied Physics* 104 (2008) 033512.
- [31] M. Tonks, D. Gaston, C. Permann, P. Millett, G. Hansen, D. Wolf, A coupling methodology for mesoscale-informed nuclear fuel performance codes, *Nucl. Engrg. Design* 240 (10) (2010) 2877–2883.
- [32] P. F. Sens, The kinetics of pore movement in UO_2 fuel rods, *Journal of Nuclear Materials* 43 (3) (1972) 293–307.
- [33] KTA rule 3102.1, Reactor core design for high-temperature gas-cooled reactor Part 1: Calculation of the material properties of helium (1978).
- [34] KTA rule 3102.2, Reactor core design for high-temperature gas-cooled reactor Part 2: Heat transfer in spherical fuel elements (1983).
- [35] KTA rule 3102.3, Reactor core design of high-temperature gas-cooled reactors Part 3: Loss of pressure through friction in pebble bed cores (1981).
- [36] IAEA, Heat transport and afterheat removal for gas cooled reactors under accident conditions, Tech. Rep. IAEA-TECDOC-1163, IAEA (2000).
- [37] F. Reitsma, K. Ivanov, T. Downar, H. de Hass, S. Sen, G. Strydom, R. Mphahlele, B. Tyobeka, V. Seker, H. Gougar, H. Lee, PBMR coupled neutronics/thermal hydraulics transient benchmark the PBMR-400 core design, Tech. Rep. NEA/NSC/DOC(2007) Draft-V07, OECD/NEA/NSC (2007).
- [38] G. Strydom, F. Reitsma, P. T. Ngeleka, K. N. Ivanov, The OECD/NEA/NSC PBMR 400MW coupled neutronics thermal hydraulics transient benchmark: transient results, *PHYSOR2010*, 2010.
- [39] B. Boer, D. Lathouwers, J. L. Kloosterman, T. H. J. J. van der Hagen, G. Strydom, Validation of the DALTON-THERMIX code system with transient analyses of the HTR-10 and application to the PBMR, *Nuclear Technology* 170 (2010) 306–321.
- [40] J. Rutqvist, Y. S. Wu, C. F. Tsang, G. Bodvarsson, A modeling approach for analysis of coupled multiphase fluid flow, heat transfer, and deformation in fractured porous rock, *Internat.*

- J. Rock Mech. and Mining Sci. 39 (4) (2002) 429–442.
- [41] K. Pruess, K. Oldenberg, G. Moridis, TOUGH2 user's guide, version 2.0, Tech. Rep. LBNL-43134, Berkeley National Laboratory, Berkeley, California (1999).
- [42] FLAC 3D, fast Lagrangian analysis of continua in 3 dimensions. version 2.0., Tech. rep., ITASCA Consulting Group (1997).
- [43] D. H. Brownell, S. K. Garg, J. W. Pritchett, Governing equations for geothermal reservoirs, *Water Resour. Res.* 13 (6) (1977) 929–934.
- [44] C. R. Faust, J. W. Mercer, Geothermal reservoir simulation .2. numerical-solution techniques for liquid-dominated and vapor-dominated hydrothermal system, *Water Resour. Res.* 15 (1) (1979) 31–46.
- [45] C. R. Faust, J. W. Mercer, Geothermal reservoir simulation .1. mathematical-models for liquid-dominated and vapor-dominated hydrothermal systems, *Water Resour. Res.* 15 (1) (1979) 23–30.
- [46] J. C. Jaeger, N. G. W. Cook, R. W. Zimmerman, *Fundamentals of Rock Mechanics*, 4th ed., 2007.
- [47] S. Garg, D. Kassoy, *Convective heat and mass transfer in hydrothermal systems*, *Geothermal Systems: Principles and Case Histories*.
- [48] T. Graf, *Simulation of geothermal flow in deep sedimentary basins in Alberta.*, Tech. Rep. Openb File Report 2009-11, ERCB/AGC (2009).
- [49] J. W. Elder, Transient convection in a porous medium, *J. Fluid Mech.* 27 (Part 3) (1967) 609–&.
- [50] C. M. Oldenburg, K. Pruess, Dispersive transport dynamics in a strongly coupled groundwater-brine flow system, *Water Resour. Res.* 31 (2) (1995) 289–302.
- [51] P. Frolkovic, H. DeSchepper, Numerical modelling of convection dominated transport coupled with density driven flow in porous media, *Adv. in Water Res.* 24 (1) (2000) 63–72.
- [52] G. T. Yeh, V. S. Tripathi, A critical evaluation of recent developments in hydrogeochemical transport models of reactive multichemical components, *Water Resour. Res.* 25 (1989) 93–108.
- [53] C. I. Steefel, K. T. B. MacQuarrie, Approaches to modeling of reactive transport in porous media, in: P. C. Lichtner, C. I. Steefel, E. H. Oelkers (Eds.), *Reactive Transport in Porous Media*, Vol. 34, *Review in Mineralogy*, 1996, pp. 83–125.
- [54] T. Xu, E. L. Sonnenthal, N. Spycher, K. Pruess, TOUGHREACT user's guide: A simulation program for non-isothermal multiphase reactive geochemical transport in variable saturated geologic media, Tech. Rep. LBNL-55460, Berkeley National Laboratory, Berkeley, California (2004).
- [55] M. D. White, M. Ostrom, STOMP (Subsurface Transport over Multiple Phases) version 2.0: Theory guide, Tech. Rep. PNNL-12030, Pacific Northwest National Laboratory, Richland, Washington (2000).
- [56] M. D. White, B. P. McGrail, STOMP (Subsurface Transport over Multiple Phases) version 1.0 addendum: Echechem equilibrium-conservation-kinetic equation chemistry and reactive transport, Tech. Rep. PNNL-15482, Pacific Northwest National Laboratory, Richland, Washington (2005).
- [57] C. Zheng, P. P. Wang, MT3DMS: A modular three-dimensional multispecies transport model for simulation of advection, dispersion, and chemical reactions of contaminants in groundwater systems; documentation and user's guide, Tech. Rep. SERDP-99-1, U. S. Army Corps of Engineers, Washington, D. C. (1999).
- [58] T. Xu, F. Gerard, K. Pruess, G. Brimhall, Modeling non-isothermal multiphase multi-species reactive chemical transport in geologic media, Tech. Rep. LBNL-40504, Ernest Orlando

- Lawrence Berkeley National Laboratory (1997).
- [59] L. Li, C. I. Steefel, L. Yang, Scale dependence of mineral dissolution rates within single pores and fractures, *Geochimica Et Cosmochimica Acta* 72 (2) (2008) 360–377.
 - [60] L. A. Warren, P. A. Maurice, N. Parmar, F. G. Ferris, Microbially mediated calcium carbonate precipitation: Implications for interpreting calcite precipitation and for solid-phase capture of inorganic contaminants, *Geomicrobiol. J.* 18 (2001) 93–115.
 - [61] Y. Fujita, G. D. Redden, J. C. Ingram, M. M. Cortez, F. G. Ferris, R. W. Smith, Strontium incorporation into calcite generated by bacterial ureolysis, *Geochemica et Cosmochimica Acta* 68 (15) (2004) 3261–3270.
 - [62] Y. Fujita, J. L. Taylor, T. L. Gresham, M. E. Delwiche, F. S. Colwell, T. L. McLing, L. M. Petzke, R. W. Smith, Stimulation of microbial urea hydrolysis in groundwater to enhance calcite precipitation, *Environmental Science & Technology*.
 - [63] A. C. Lasaga, *Kinetic Theory in the Earth Sciences*, Princeton Univ. Press, Princeton, N. J., 1998.
 - [64] M. Fialeo, R. Lavecchia, Kinetic study of enzymatic urea hydrolysis in the pH range 4–9, *Chemical Biochemical Engineering Quarterly* 17 (4) (2003) 305–318.
 - [65] T. J. Wolery, EQ3/6, A software package for geochemical modeling of aqueous systems: Package overview and installation guide (version 7.0), Tech. Rep. UCRL-MA-110662 PT I, Lawrence Livermore National Laboratory (1992).
 - [66] S. B. Yabusaki, Y. Fang, S. R. Waichler, Building conceptual models of field-scale uranium reactive transport in A dynamic vadose zone-aquifer-river system, *Water Resour. Res.* 44 (W12403).
 - [67] B. W. Bader, R. P. Pawlowski, T. G. Kolda, Robust large-scale parallel nonlinear solvers for simulations, Tech. Rep. SAND2005-6865, Sandia National Laboratories (2005).
 - [68] E. D. Fichtl, J. S. Warsa, J. D. Densmore, The Newton-Krylov method applied to negative-flux fixup in *SN* transport calculations, *Nuclear Science and Engineering* 165 (3) (2010) 331–341.
 - [69] H. Park, R. Nourgaliev, D. Knoll, Jacobian-Free Newton-Krylov Discontinuous Galerkin (JFNK-DG) method and its physics-based preconditioning for all-speed flows, in: *Bulletin of the American Physical Society, 60th Annual Meeting of the Division of Fluid Dynamics*, Vol. 52, American Physical Society, 2007, abstract: GB.00004, <http://meetings.aps.org/link/BAPS.2007.DFD.GB.4>.